Biomaterials Science

ROYAL SOCIETY OF CHEMISTRY

PAPER

View Article Online
View Journal | View Issue

Cite this: *Biomater. Sci.*, 2023, **11**, 140

A lipid–polymer hybrid nanoparticle (LPN)-loaded dissolving microneedle patch for promoting hair regrowth by transdermal miR-218 delivery†

Yipu Zhao,[a,b,c] Ye Tian,[a,b,c] Weiliang Ye,[d] Xue Wang,[a,b,c] Ying Huai,[a,b,c] Qian Huang,[a,b,c] Xiaohua Chu,[a,b,c] Xudong Deng *[a,b,c] and Airong Qian *[a,b,c]

Received 7th September 2022,
Accepted 2nd November 2022

DOI: 10.1039/d2bm01454h

rsc.li/biomaterials-science

Alopecia is the most common multifactorial hair loss disorder, affecting almost 50% of the population and even having a serious psychological impact on the patients. miR-218 has therapeutic potential for alopecia since it can activate the Wnt/β-catenin channel by down-regulating SFRP2, which is a key channel in hair follicle cycle transformation for hair regrowth. Although miR-218 has the potential to treat this disease, several barrier properties of the skin challenge miRNA's delivery to the target location, such as passing through the corneum and resistant enzymatic degradation. To address these challenges, we evaluated a device that combined the use of hyaluronic acid (HA)-based dissolving microneedle (MN) to enhance corneum permeability with the lipid polymer hybrid nanoparticles (LPNs) as a miRNA delivery carrier to protect miR-218 from degradation. The MN patches could promote LPNs/miR-218 diffusing in the dermis region, and significantly increase the bioavailability of miR-218. Furthermore, in the shaved mouse model, the MN patches showed higher efficacy in promoting hair growth than the topical smear treatment, while avoiding the safety concern. This work established a novel and effective combination device with MN and LPNs that can be used for localized transdermal miRNA delivery to promote hair regrowth.

1. Introduction

Recently, numerous causes determining the occurrence of alopecia have been identified, such as medications' side effects, hormonal dysfunction, and environmental impact.[1] It is estimated that more than 50% of the general population suffers from hair loss both in men and women, which has been associated with psychological impacts.[2] For this extremely high-incidence disorder, the current clinical treatment mainly relies on hair follicle transplantation or FDA-approved drugs, finasteride and minoxidil.[3] The transplantation is confined to the exorbitant expense and invasive surgery,[4] and the FDA-approved drugs reveal limited usage due to the concerns of side effects and partial efficacy.[5] Therefore, a noninvasive and secure solution inducing hair regrowth is highly demanded.

Replenishment of dermal papilla (DP) cells is a plausible way to induce hair regrowth in alopecia patients.[6] As a crucial part of physiology, cycling intact of the hair follicle maintains the proliferation dynamics or creates perturbation during responses to different factors.[7] The hair follicle cycle undergoes three phases, active growing (anagen), regression (catagen), and resting (telogen) to provide new hairs, persistently.[8] During the anagen phase, the DP cells are in a state of proliferation and differentiation, after that the catagen phase is a short transition state of hair growth culmination through the apoptosis of DP cells that leads to hair follicle regression. Finally, in the telogen phase, the hair follicle remains in long dormancy before starting a new cycle.[9] Therefore, a large number of differentiated DP cells could meet the telogen-to-anagen phase transition needed for hair follicles and further promote hair regeneration.[10] There have been reports confirming the regulatory impact of miR-218 in promoting the division and proliferation of DP cells by down-regulating secreted frizzled-related protein (SFRP2), an inhibitor of the Wnt/β-catenin channel.[11,12]

In this study, we propose to the transdermal deliverer of miR-218 for facilitating the proliferation of DP cells and ultimately promoting hair regrowth. However, the miRNA

[a]*Lab for Bone Metabolism, Xi'an Key Laboratory of Special Medicine and Health Engineering; Key Lab for Space Biosciences and Biotechnology, School of Life Sciences, Northwestern Polytechnical University, Xi'an, Shaanxi, China*
[b]*Research Center for Special Medicine and Health Systems Engineering, School of Life Sciences, Northwestern Polytechnical University, Xi'an, Shaanxi, China*
[c]*NPU-UAB Joint Laboratory for Bone Metabolism, School of Life Sciences, Northwestern Polytechnical University, Xi'an, Shaanxi, 710072, China. E-mail: dengxd@nwpu.edu.cn, qianair@nwpu.edu.cn*
[d]*Department of Pharmaceutics, School of Pharmacy, Fourth Military Medical University, Xi'an, China*

† Electronic supplementary information (ESI) available. See DOI: https://doi.org/10.1039/d2bm01454h

transdermal strategy, which enables the direct access of therapeutic miRNA to the dermis region in the scalp without going through the circulatory system, is limited by the low stability and electronegativity of naked miRNAs.[13,14] For achieving efficient therapy, miRNA should resist enzymatic degradation, enter cells and escape from lysosomes in the cytoplasm successfully. Herein, lipid/polymer hybrid nanoparticles (LPN)s endowed with the holonomic constraint of miRNA in the core were synthesized. LPN is a promising delivery carrier with a core–shell structure and physicochemical stability since it integrates the biomimetic advantages of liposomes and the tolerability of polymeric nanoparticles.[15,16] In the LPN formulation, cholesterol and natural saturated phospholipid lecithin were used to stabilize the structure of LPNs, as in cellular membranes;[17] the outer DSPE-PEG (distearoyl phosphoethanolamine-polyethylene glycol) layer was used as a stealth coating to prolong the *in vivo* circulation time;[18] the cationic polymer polyvinylamine (PVAm) was utilized as a core to facilitate endosomal escape in which the therapeutic miRNAs were encapsulated.[19–21] Furthermore, the stratum corneum is another vital hurdle of transdermal RNA therapy. A microneedle (MN) patch, a promising transdermal device, was flexibly adjusted to fit irregular skin surfaces and to achieve different depths of delivery.[22,23] Of the various MNs types, the dissolving MN, supported by water-soluble matrix materials and absorbed cutaneous tissue fluids after insertion, has distinct advantages of no risk of needle re-insertion and no requirement for sharps disposal.[24–26] Hyaluronic acid (HA) is an inherent component of the skin with excellent security, as a dissolving MN matrix material, it can regulate drug release by controlling the matrix material's dissolution rate to achieve accurate drug delivery.[19] In summary a combination of dissolving MN patches with LPNs was utilized to penetrate the corneum and deliver painlessly miRNAs through the microchannels of MN into the deep skin region.[27,28] In view of this, the dissolving HA-based MN transdermal patch-integrated LPNs delivered miR-218 for activating the Wnt/β-catenin channel, which promoted the proliferation and differentiation of DP cells, and further regulated the hair follicle cycle transition, eventually facilitated hair regrowth.

2. Materials and methods

2.1 Materials

Polyvinylamine (PVAm) polymer (Xelorex™ RS 1100) was provided by BASF (China) Co. Ltd (Shanghai, China). DSPE-PEG, cholesterol, and lecithin were obtained from Ruixibio (Xi'an, China). Hyaluronic acid was purchased from Freda (Shandong, China). Rhodamine B dye was obtained from Sigma (USA). miR-218 and its negative control MSA were provided by RQCON Biological Technology Co., Ltd (Xi'an, China). LysoTracker Red was obtained from Beyotime (Beijing, China). FAM-miR-218 were obtained from GenePharma (Shanghai, China). Cy5 was obtained from Meilunbio (Dalian, China). 3-(4,5-Dimethylthiazol-2-yl)-2,5-diphenyltetrazolium bromide (MTT) was purchased from Solarbio (Beijing, China). Antibodies against Wnt-3a (A0642), SFRP2 (A5383), and LRP6 (A13324) were purchased from Abclonal (Wuhan, China), anti-β-catenin (D10A8) was purchased from CST (Boston, USA), anti-GAPDH (10494-1-AP) was purchased from Proteintech (Wuhan, China). Antibody Goat-anti-rabbit IgG Alexa Fluor488 was got from Zhuangzhi Biotechnology (Xi'an, China). In all experiments, Milli-Q grade distilled deionized water was used.

2.2 Preparation of LPNs

LPNs were typically prepared by evaporation-emulsification using a two-step method. Briefly, 3 μL lecithin (50 nmol), 1.5 μL cholesterol (50 nmol), and 4 μL DSPE-PEG (1 nmol) lipid mixture were fully dissolved in 3 mL chloroform, followed by evaporation in a rotary evaporator (QYRE-501, QiYu, China) to form a dried thin lipid film. Simultaneously, 1 mL nuclease-free HEPES (pH 6.5) suspension containing PVAm/miR-218 complexes was added to the above lipid film (PVAm : miR-218 = 1 : 2, w/w), while the PVAm was added to the lipid mixture at a ratio of 10 : 1 (w/w). After that, pre-LPNs were fully hydrated for 30 min and treated under ultrasonication under 100 W for 10 min.[29] For the LPNs/FAM-miR-218 preparation, the FAM-miR-218 was utilized.

2.3 Characterization of LPNs/miR-218

Dynamic light scattering (DLS). LPNs were prepared under different optimized parameter conditions. The size of LPNs measured using DLS and ξ-potential measurements using Nano-ZS analyzer (Nano ZS/ZEN3600, Malvern Panalytical, UK) instruments, respectively, at 25 °C. The sizes and ξ-potentials of LPNs were calculated automatically.

Agarose gel retardation assay. miR-218 with different amounts of LPNs were prepared by adding appropriate volumes of the LPNs to 10 μL of miR-218 (300 μg mL^{-1}). After incubation for 20 min at room temperature. The samples were electrophoresed on a 1% (w/v) agarose gel containing GelRed™ in Tris-acetate (TAE) running buffer at 120 V for 15 min. The RNA was visualized using the Tanon 4600SF gel imaging system (Tanon Science & Technology Co., Ltd, Shanghai, China). In order to evaluate the protection and preservation of LPNs to RNA following the systemic administration and MN backbone HA, LPNs/miR-218 or naked miR-218 were incubated with 10% FBS (v/v) or 20% HA at 37 °C for 1, 3, 5, 7, 9, 24, and 48 h. Then, the mixtures were loaded on 1% agarose gel followed by electrophoresis, and the RNA integrity was visualized by gel documentation.

Morphology of LPNs. The morphology of LPNs was observed by transmission electron microscopy (TEM, TECNAI Spirit G2, Thermo Fisher, USA). TEM images were obtained at an acceleration voltage of 200 kV and with phosphotungstic acid staining.

2.4 Transfection of LPNs/miR-218

One day before transfection, DP cells were seeded in a 24-well plate at a density of 1×10^5 cells per well in 0.5 mL in a culture

medium. After removing the culture medium, cells were incubated with 400 μL Opti-MEM™ medium and freshly made vehicle (LPNs or Lipo2000) miRNA mixture (100 μL total volume, equal to miR-218 or MSA = 20 nM) were added to each well. Lipo2000 was used as a positive control vehicle.

Western blotting. After 24 h treatment with different nanoparticles, cells were harvested and washed twice with cold PBS. Cell lysates were prepared in RIPA buffer (Beyotime, Shanghai, China) supplemented with 1% protease inhibitor Cocktail Set III (Valbiochem, Darmstadt, Germany) on ice. Protein concentrations were determined using a BCA Protein Assay Kit (Thermo Fisher Scientific, USA). Whole-cell proteins (50 μg per lane) were loaded and resolved on a 10% SDS-PAGE, then transferred onto PVDF membranes. The membranes were blocked for 1 h in 5% skim milk in TBST buffer, then immunoblot was performed by incubating the membranes with anti-Wnt-3a, anti-SFRP2, anti-LRP6, anti-β-catenin, and anti-GAPDH rabbit antibody. Then, the membranes were incubated with secondary antibodies (goat anti-rabbit IgG) conjugated with horseradish peroxidase for 3 h at room temperature. After being incubated with Clarity Western ECL substrates (Bio-Rad), the protein bands were detected by Tanon 4600SF gel imaging system (Tanon Science & Technology CO., Ltd, Shanghai, China).

Reverse transcription quantitative real-time PCR (RT-qPCR) and stem-loop RT-qPCR. After 24 h of transfection with nanoparticles containing miR-218 or negative control miRNA (MSA), total RNAs of cells were isolated with E.Z.N.A.® Total RNA Kit II (Omega Bio-tek, Inc. Norcross, GA). The cDNAs were synthesized using HiScript II Q RT SuperMix (Vazyme Biotech, China) with random hexamers. qPCR analyses were carried out using SYBR Green Master Mix (Vazyme Biotech, China) and gene-specific primers on a CFX96 Touch real-time PCR system (Bio-Rad, Hercules, CA). U6 and GAPDH were used as internal controls for miRNA and mRNA levels, respectively. Cells were treated in triplicate and assayed separately. The comparative threshold cycle (Ct) method with the formula $2^{-\Delta\Delta Ct}$ was used to calculate the relative gene expression.

Stem-Loop RT-qPCR was used to detect the intracellular level of mature miR-218. The primers for stem-loop RT-qPCR were designed according to the previous report.[30] The primer sequences are shown in Table 1.

Lysosomal escape assay. DP cells were seeded in the covered glass containing 24-well plates at a density of 50% proportion cells per well in 0.5 mL total culture medium overnight. After removing the culture medium, the cells were incubated with 400 μL DMEM medium (containing 3% FBS), and freshly made LPNs 100 μL (10 μL FAM-miR-218 as final concentrations of 20 nM and 90 μL LPNs) were added to each well. After 4 h incubation, the cells were rinsed three times with PBS and stained with lysotracker Red (100 nM, Beyotime, C1046, China) and 2× Hoechst 33342 (H3570, Invitrogen, USA) for 15 min. After that, the cells were fixed with 4% paraformaldehyde. The fluorescence of the cells was observed by CLSM. Three parallel samples were prepared for each experiment by avoiding light during the whole experiment.

Table 1 Primer sequence

Stem-loop reverse transcription primer	5′-GTCGTATCCAGTGCAGGGTCCGA GGTATTCGCA CTGGATACGACACATGG-3′
mmu-miR-218-F	5′-CACGCATTGTGCTTGATC-3′
mmu-miR-218-R	5′-CCAGTGCAGGGTCCGAGGTA-3′
mmu-U6-F	5′-GTGCTCGCTTCGGCAGCACATAT-3′
mmu-U6-R	5′-AAAATATGGAACGCTTCACGAA-3′
mmu-GAPDH-F	5′-CCTCTGACTTCAACAGCGAC-3′,
mmu-GAPDH-R	5′-TCCTCTTGTGCTCTTGCT GG-3′
mmu-SFRP2-F	5′-ACGGCATCGAATACCAGAACA-3′
mmu-SFRP2-R	5′-CTCGTCTAGGTCATCGAGGCA-3′
mmu-Wnt-3a-F	5′-TGCCGATGCCAGGGAGAACC-3′
mmu-Wnt-3a-R	5′-CCAGCAGGTCTTCACTTCACAGC-3′
mmu-β-catenin-F	5′-ACGCTGCTCATCCCACTAAT-3′
mmu-β-catenin-R	5′-AGTTCCGCGTCATCCTGATA-3′
mmu-LRP6-F	5′-GCTTCTGCGTGCTGCTGAGAG-3′
mmu-LRP6-R	5′-CCTCCAAGCCTCCAACTACAATCG-3′

2.5 Fabrication of LPNs-loaded MN patch

To minimize drug wastage, LPNs/miR-218 were only loaded in the MN tips. The MN molds were fabricated in 10 × 10 arrays through a mold-casting method.[31] Briefly, arrays of microneedle master structures were fabricated by stainless steel using laser cutting, and then an inverse mold was created by casting the master structures in polydimethylsiloxane (PDMS). After that, the hydrosoluble backbone HA was mixed with LPNs/miR-218 until homogenous (20 μg miR-218 each patch), and 200 μL of the blend was dispensed into the holes of the PDMS model. Then, the models were placed in a negative pressure chamber for 10 min to fill the cavities. Finally, MNs were forced-air dried at 35 °C for 10 h, and a protective layer with the 20% w/v HA was placed behind the MNs formulation, the same drying conditions were applied (Fig. 3A). For the Gel/LPNs/miR-218 group, a homogenous mixture of 100 μL of HA and LPNs/miR-218 (20 μg miR-218 each sample) was utilized on the skin without air drying, directly.

2.6 Morphologies and physical properties of LPNs-loaded MN

The morphology of the MN was observed using a microscope (WMF-3580, YuGuang, China) and a scanning electron microscope (SEM, VEGA-3-SBH, Tescan, CZ). The mechanical fracture force of LPNs-loaded MN was assessed using a universal tester (HY-1080, HengYi, China). Briefly, after a single LPNs-loaded MN patch was separated and attached to the detection station of the force machine, the axial force was recorded when the sensor probe was pressed onto the tips of LPN-loaded MN in a downward vertical direction at speed of 10 μm s^{-1}. A compression test of LPN-loaded MN was also performed using the universal tester. Briefly, MNs with different LPN content were attached to the detection station and then pressed against a 40 N force for 5 s from the contact. The pre- and post-test speeds were both set at 10 μm s^{-1}. Tips height of the LPN-loaded MNs were imaged and recorded, and the percentage of the change in the height of the needles after compression was calculated.

In addition, to detect the stability of miR-218 in the MN patch with or without LPNs, e MN/miR-218 and MN/LPNs/

miR-218 (20 μg miR-218/MN) were prepared and re-dissolved in 1 mL DEPC water at 1, 3, 5, 10, 20, 30-days after preparation. Then, the miR-218 concentration was tested using the RediPlate™ 96 RiboGreen® RNA Quantitation Kit, and 0.5% Triton was added to the MN/LPNs/miR-218 group for destroying the lipid layer before detection.

2.7 Cutaneous penetration of MN

In order to visualize the cutaneous penetration ability of MN, the fluorescence Cy5 was used as a cargo loaded into MN or Gel, abbreviations for MN/Cy5 and Gel/Cy5. Firstly, MN/Cy5 and Gel/Cy5 were applied on the hair-removed rat dorsal skin for 5 min (10 μg Cy5 for each mouse). The mice were imaged on pre-treatment, and 5 or 10 min after treatment, under the Caliper IVIS Lumina II imaging system (Caliper Life Sciences Inc., Waltham, MA, USA) with an excitation wavelength of 650 nm and emission wavelength of 670 nm. The fluorescence intensity in each joint was calculated using Living image ® version 4.3.1 software. On the other hand, Franz diffusion cells with full-thickness rat dorsal skin were used to detect the depth of penetration. The skin was shaved and pre-equilibrated in PBS (pH 7.4) for 15 min and then attached to Franz diffusion cells. The receiver compartment was filled with PBS (pH 7.4) and stirred at 500 rpm for 36 °C. MN/Cy5 were inserted into the skin using manual force to ensure that the MN remained in place for the experiment. Meanwhile, Gel/Cy5 was smeared on the skin. At the predetermined time intervals of 6 h and 24 h, and MN/Cy5 and Gel/Cy5 were removed and the skin was washed with deionized water to clear the surface residue and tissue slicing for the skin.

2.8 *In vivo* pharmacokinetics of MN/LPNs

In this study, 6–8 weeks-old mice were randomly divided into the Gel smear group and MN group, with 3 mice in each group. The Gel group was administered with LPNs-miR-218 (20 μg miR-218 each mouse) suspension of 100 μL HA Gel to make it homogeneous. The MN-administration group was topically administered with one patch (20 μg miR-218 each pitch) on the dorsal skin of each mouse. 1 cm × 1 cm dorsal skin and 1 mL blood samples were taken from mice at 15 min, 45 min, 2 h, 8 h, 24 h, and 48 h for each group after one-time administration. The samples were extracted for mRNA and mature miR-218 expression was detected by stem-loop RT-PCR. To analyze the pharmacokinetics profiles, Phoenix WinNonlin 8.1 was utilized with a non-atrioventricular model after the construction of a curve consisting of the drug concentration time. Several parameters were observed, such as maximum drug concentration (C_{max}), time of maximum concentration (t_{max}), the area under the drug concentration–time curve from the beginning to the last time point (t = 48 h) (AUC), and the mean residence time (MRT).

2.9 Animal experiments

To evaluate the hair growth promotion, 6–8 weeks old C57BL/6J mice under sugaring hair removal were used. All animal procedures were performed in accordance with the Guidelines for Care and Use of Laboratory Animals of Northwestern Polytechnical University and approved by the Animal Ethics Committee of Northwestern Polytechnical University. On the following day of the hair removal, the mice were divided into four groups: control (non-treated group), Gel/LPNs/miR-218, MN/LPNs/MSA and MN/LPNs/miR-218 (equal to miR-218 = 20 μg per mouse). In the Gel/LPNs/miR-218 group, 50 μL of 20% HA gel mixed with equal LPNs/miR-218 was applied to 1 cm × 1 cm of the dorsal skin. The patch was pressed firmly for 10 s to penetrate through the epidermis. Both the administrations of each group were performed every 4 days and continued for 13 days. The hair phenotype transformation was studied through real-time observation of hair regrowth in mice. After the experiment, hair in different groups was harvested and observed using a scanning electron microscope (SEM, VEGA3 SBH, Tescan, USA), and the thicknesses of new hair were measured using the ImageJ software. The skin tissues were excised from the shaved dorsal area and fixed in 4% paraformaldehyde. Paraffin was employed to embed the sample. Then, the skin tissues were cut into slices of 4 μm along the sagittal plane and stained with H&E to evaluate the condition of the hair follicle. Meanwhile, the length of the hair follicle was detected using the ImageJ software and calculated using GraphPad prism 7.0. For the immunofluorescence assay, fresh skin tissue sections were fixed in 4% paraformaldehyde for 1 h and blocked in PBS containing 10% bovine serum albumin at 25 °C for 30 min. Then, the sections were incubated overnight at 4 °C with primary antibodies SFRP2 (1 : 100) and β-catenin (1 : 100). After incubation, the sections were rinsed with PBS and incubated with the secondary antibody of Alexa Fluor 488 (1 : 200) at 25 °C for 1 h and counterstained with Hochest 33342 (1 : 1000). The fluorescent signals were visualized using a fluorescence microscope (Observer 3, ZEISS, Germany) and the relative fluorescence intensity was measured by ImageJ software. Furthermore, the proteins and mRNA from the skin tissues of each group were extracted and prepared for WB and RT-qPCR detection.

2.10 Statistical analysis

SPSS13.0 software was used to analyze the datum. Results were expressed as mean ± SD. In all experiments, the error bar indicates SD. Significance was determined using a one-way analysis of variance (ANOVA) followed by Dunnett's test. $P < 0.05$ was considered statistically significant (GraphPad).

3. Results and discussion

3.1 Preparation and characterization of LPNs/miR-218

As shown in the composition schematic of LPNs/miR-218 (Fig. 1A), the cholesterin, lecithin and DSPE-PEG consisted of the lipid layer. Meanwhile, PVAm condensed miR-218 in the LPNs through the electrostatic interaction. Based on the evaporation-emulsification two-step preparation method, the lipid composition ratio, PVAm : lipid mass ratio, hydration volume of 2-[4-(2-hydroxyethyl)-1-piperazinyl] ethanesulfonic acid

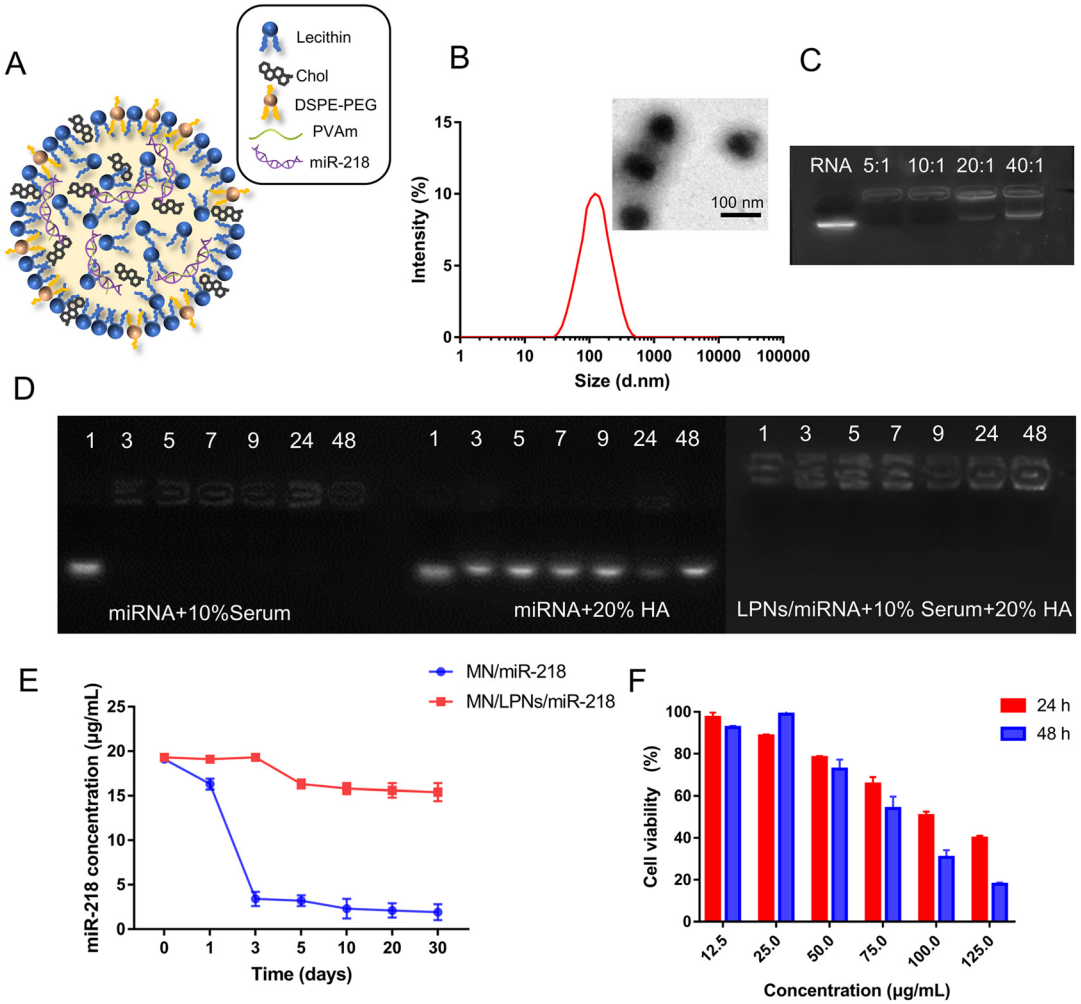

Fig. 1 Characterization of the LPNs. (A) Schematic representation of LPNs/miR-218. (B) DLS and TEM images of LPNs/miR-218 (scale bar = 100 nm). (C) Gel retardation assay of LPNs/miR-218 under different WR (miR-218 : lipid = 5 : 1, 10 : 1, 20 : 1, 40 : 1). (D) Gel retardation assay for the stability of LPNs/miR-218 (miR-218 : lipid [WR] = 20 : 1) following incubation in 10% (v/v) mouse serum combine with 20% HA for different times, and naked miR-218 incubation in 10% (v/v) mouse serum or 20% HA, respectively. (E) miR-218 residual concentration in MN/miR-218 and MN/LPNs/miR-218 patches under different times. (F) MTT assay to detect the cellular toxicity of LPNs on DP cells, n = 5. Data were shown as the mean ± SD and the statistical significance was calculated by one-way ANOVA followed by Dunnett's test.

(HEPES) solution and hydration time were detected to optimize the preparation method. As shown in Table 2, with the increase of the DSPE-PEG proportion, the size of LPNs was decreased slightly accompanied by no significant influences on the zeta and PDI values, from which the lipid 50 : 50 : 1 composition ratio of cholesterin : lecithin : DSPE-PEG, respectively, was utilized. Generally, the PEGylated lipid was employed to stabilize the LPNs' structure and regulate the size, and a smaller size of LPNs was generated by higher PEGylated lipid ratio,[32] which was consistent with our experimental results. According to our previous studies, PVAm is a kind of safety cationic polymer with high efficiency for RNA delivery,[33] which was used to condense miR-218 in the core of LPNs. The excess of PVAm tended to form PVAm/miR-218 complexes without the lipid shell deteriorated the homogeneity of LPNs and concurrently led to larger PDI values, while the overcapacity of the lipid mixture shell might cause particle oversize.[34,35] Hence, PVAm : lipid = 10 : 1, respectively, was chosen for LPN preparation. In addition, with a large amount of the HEPES buffer solution added during the hydration process, the formed LPNs/miRNA were self-assembled into stable particles with the solvent-switching effect of chloroform/water, adequately.[36] The suitable hydration volume and hydration time could provide self-assembly surroundings. On the basis of the smaller particle size and better uniformity, 1 mL of HEPES volume and 0.5 h hydration time were chosen for LPNs fabrication. Under the optimize parameters preparation, dynamic light scattering (DLS) was used to measure the size of LPNs, which was 141 ± 14 nm with PDI of 0.16 ± 0.04 and the zeta potential of 5.34 ± 1.06 mV (Fig. 1B). Moreover, the nanostructure of LPNs was further characterized by transmission electron microscopy (TEM). As shown from the images of TEM (Fig. 1B), LPNs

Table 2 Optimize parameters for the LPN formulation

Optimize condition		Size (nm)	PDI	Zeta (mV)
Cholesterin : lecithin : DSPE-PEG (n/n)	50 : 50 : 1	148 ± 15	0.14 ± 0.02	5.15 ± 2.31
	50 : 50 : 10	142 ± 13	0.16 ± 0.03	6.24 ± 1.74
	50 : 50 : 30	126 ± 28	0.17 ± 0.02	5.62 ± 2.03
PVAm : lipid (w/w)	10 : 0.5	125 ± 21	0.42 ± 0.16	1.36 ± 0.28
	10 : 1	134 ± 21	0.11 ± 0.02	1.14 ± 0.34
	10 : 2	182 ± 35	0.24 ± 0.13	5.72 ± 1.46
HEPES (mL)	4	294 ± 45	0.37 ± 0.13	3.42 ± 1.27
	2	204 ± 21	0.35 ± 0.12	2.67 ± 1.07
	1	156 ± 20	0.15 ± 0.03	5.32 ± 1.48
Hydration time (h)	3	143 ± 16	0.16 ± 0.03	6.21 ± 1.32
	0.5	153 ± 14	0.15 ± 0.02	5.79 ± 1.45

revealed a solid spherical morphology with uniform size distribution.

Agarose gel electrophoresis was performed to investigate the miR-218 loading in LPNs. When the weight ratio (WR) of miR-218 : lipid reached a 20 : 1 value, the miR-218 was loaded totally and a little free miR-218 band was observed in Fig. 1C. Agarose gel electrophoresis was also carried out to confirm the stability of LPNs, both in serum and MN backbone HA solution. As shown in Fig. 1D, the band of the naked miR-218 was turned blurred within 1 h in 10% serum, rapidly, whereas it remained stable in 20% HA solution until 48 h, which verified the fitness of HA as the MN backbone for miRNA's transdermal delivery. On the contrary, when miR-218 was incorporated into the LPNs, there was almost no degradation in both 10% serum and 20% HA solution during 48 h. Furthermore, the stability of miR-218 in the MN patch with or without LPNs was detected at different times. As shown in Fig. 1E, after 30 days, the concentration of miR-218 was only decreased to 15 μg mL^{-1} under the protection of LPNs in the MN patch, on the contrary, without LPN protection, the naked miR-218 directly decreased to 5 μg mL^{-1} in 3 days. These indicated the protection of LPNs for miR-218 from RNase degradation. What is more, there was almost no change of miR-218 concentration in the first time point of MN/LPNs/miR-218 group which proved little effect on LPNs' structure or degradation of miR-218 by microneedle preparation method. The safety of LPNs/miR-218 is one of the important indicators for ideal gene vectors. To compare the cytotoxicity of LPNs/miR-218, MTT assays were performed at different concentrations. As shown in Fig. 1F, the viability of DP cells after LPNs/miR-218 incubation was more than 80% within the working concentration (<50 μg mL^{-1}) following time dependence and concentration dependence. Therefore, LPNs/miR-218 could maintain negligible cytotoxicity below 50 μg mL^{-1}. The above results confirmed that the optimized LPNs/miR-218 were constructed with homogeneous morphology, excellent stability, and guaranteed security.

3.2 *In vitro* transfection efficiency of LPNs/miR-218

miR-218 acted as an activator of the Wnt/β-catenin channel to promote the proliferation and division of DP cells by down-regulating Wnt/β-catenin channel inhibitor SFRP2.[12] In Fig. 2A, the mature miR-218 expression level in different groups was examined by qRT-PCR on the primary DP cells of mice. The well-established transfection reagent Lipofectamine™ 2000 (Lipo2000) was used as a positive control for miR-218 transfection *in vitro*. The expression of mature miR-218 in the LPNs/miR-218 group was higher than that in the Lipo2000/miR-218 group, which confirmed the better transfection efficiency of LPNs. Moreover, the Wnt/β-catenin channel marker, β-catenin, Wnt-3a, LRP2, and miR-218 target gene SFRP2 were also detected after miR-218 transfection for 24 h. There was a more significant elevation of β-catenin and Wnt-3a expression in the mRNA level both in Lipo2000/miR-218 and LPNs/miR-218 group than in the control group. As LPNs could bring more miR-218 into the DP cells, the expression of SFRP2 was the lowest in the LPNs/miR-218 group (Fig. 2B). In addition, the more obvious changes in β-catenin, Wnt-3a, LRP2, and SFRP2 protein levels were detected in the LPNs/miR-218 group than in Lipo2000/miR-218 (Fig. 2C). Furthermore, compared with the control group, the DP cells' proliferation of miR-218 transfected groups was significantly increased, especially, since the LPNs/miR-218 group had a higher proliferation ratio compared to other groups (Fig. 2D). Finally, the transfection efficiency of LPNs/miR-218 was also detected under different cell types, both in the tumor cell line (MDA-MB-231) and pre-osteoblast (MC3T3-E1), the mature miR-218 expression level was higher than that in the Lipo2000/miR-218 group (Fig. S1†). In summary, LPNs/miR-218 could be more efficiently internalized than Lipo2000/miR-218, which suppressed SFRP2 and activated the Wnt/β-catenin channel, thereby promoting more proliferation of DP cells. Moreover, the lysosome escape ability of LPNs was confirmed, as shown in Fig. 2E. After 4 h of incubation, cytoplasmic green (FAM-miR-218) and red (endolysosomes) fluorescence values were greatly separated, leading to low co-localized fluorescent intensity (yellow) around the nucleus, which evidenced the maintenance of LPNs in mediating lysosomal escape like PVAm.[33]

3.3 Fabrication and characterization of MN/LPNs/miR-218

The dissolvable material HA was selected as matrices for MN because it is a skin intrinsic composition with high security.[37,38] Various molecular weights and solubility of HA were tried, as shown from the data in Table 3. Depending on whether the MN matrices can be formed, 1×10^5 molecular

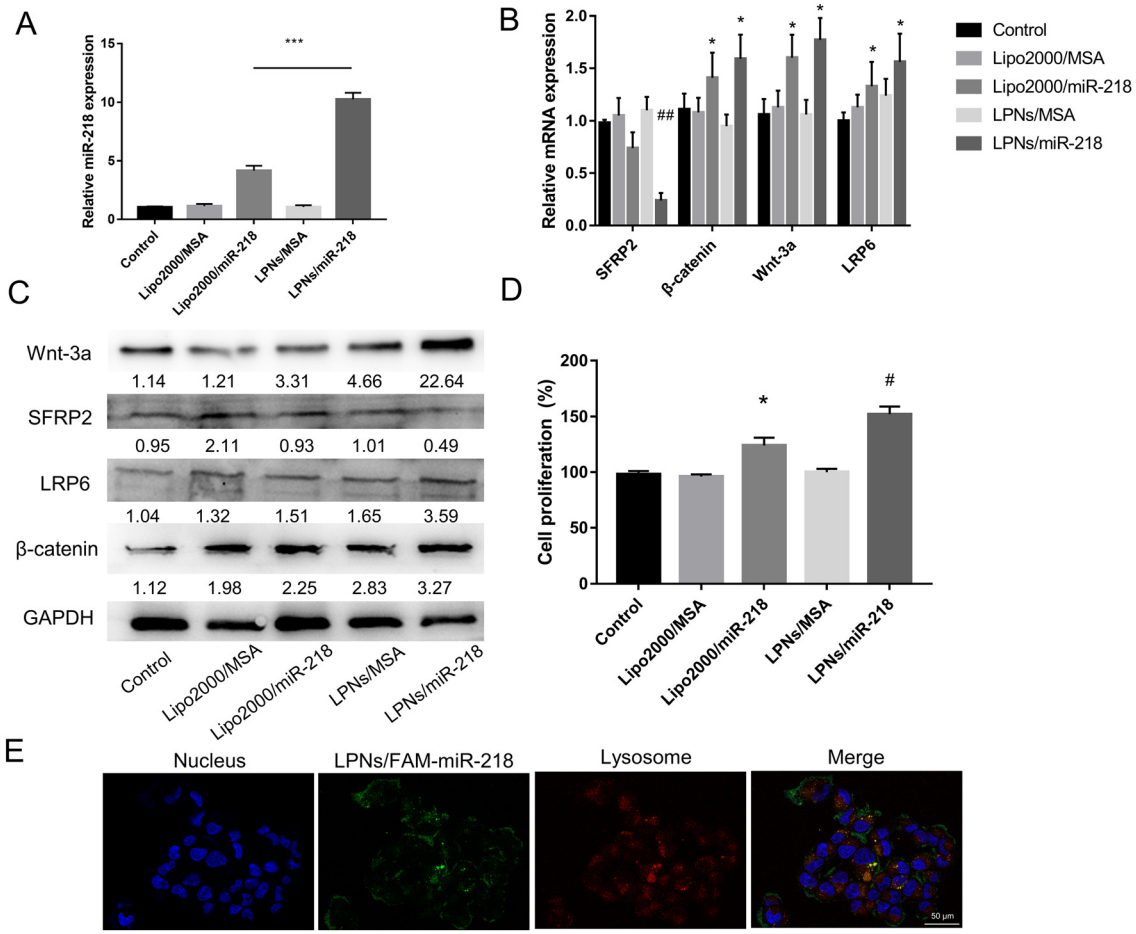

Fig. 2 Intracellular uptakes of LPNs/miR-218. The mRNA level of mature miR-218 (A), mRNA (B), and protein (C) levels of Wnt-3a, β-catenin, LRP6, and SFRP2 in DP cells after transfection, $^{***}P < 0.005$ and $^{\#\#}P < 0.01$ *vs.* Lipo2000/miR-218, $^{*}P < 0.05$ *vs.* Control. (D) The cell proliferation of DP cells after different transfection, $^{*}P < 0.05$ *vs.* Control and $^{\#}P < 0.05$ *vs.* Lipo2000/miR-218. (E) Confocal laser microscope (CLSM) images of cells treated with LPNs/FAM-miR-218 for 4 h (blue = nuclei; red = lysosomes, stained with Lysotracker Red; green = FAM-miR-218, scale bars = 50 μm). Data were shown as mean ± SD (n = 5), and statistical significance was calculated by one-way ANOVA followed by Dunnett's test.

Table 3 Formulation compositions for HA-based MNs

Code	Molecular weight	Composition% (w/v)	State
M1	1×10^6	<1%	Unsolvable
M2	1×10^5	10%	Low solvable
M3		5%	√
M4	1×10^4	20%	√
M5		15%	√
M6		10%	√
M8	1×10^3	>30%	Incoagulable

weight HA with 5% solubility, 1×10^4 molecular weight HA with 20% solubility, 1×10^4 molecular weight HA with 15% solubility, and 1×10^4 molecular weight HA with 10% solubility were chosen for further fabrication. The preparation process and MN product are shown in Fig. 3A–C. The molecular weight of HA exerted influences on the solubility and mechanical strength of MN patched.[39,40] As shown in Fig. 3D, the side view of the MN showed the remaining undissolved portions at different insertion times. Before insertion into the skin, the sharp tips of the MN body can be observed in each group. After 2 min of insertion into the skin, the needle became blunt, and the MN body was gradually dissolved to half of before height. Finally, MN, which consisted of HA with 1×10^4 of molecular weight, could be completely dissolved within 10 min, whereas a small amount of needle body remained in the 1×10^5 molecular weight group due to the difference in the solubilities of HAs with different molecular weights. In the mechanical strength testing (Fig. 3E), the force of MN in the 1×10^4 molecular weight group was higher than that in the 1×10^5 molecular weight group, especially, since the 1×10^4 molecular weight HA with 20% solubility exhibited the highest force of ~6 N, ensuring a sufficient stiffness for the skin insertion. Depending on the solubility and mechanical strength, 1×10^4 molecular weight HA with 20% solubility was chosen for further MN fabrication. Generally, the unseemly cargo loading would decrease the mechanical strength of MN and fail to penetrate through corneum.[41] Hence, the pressure

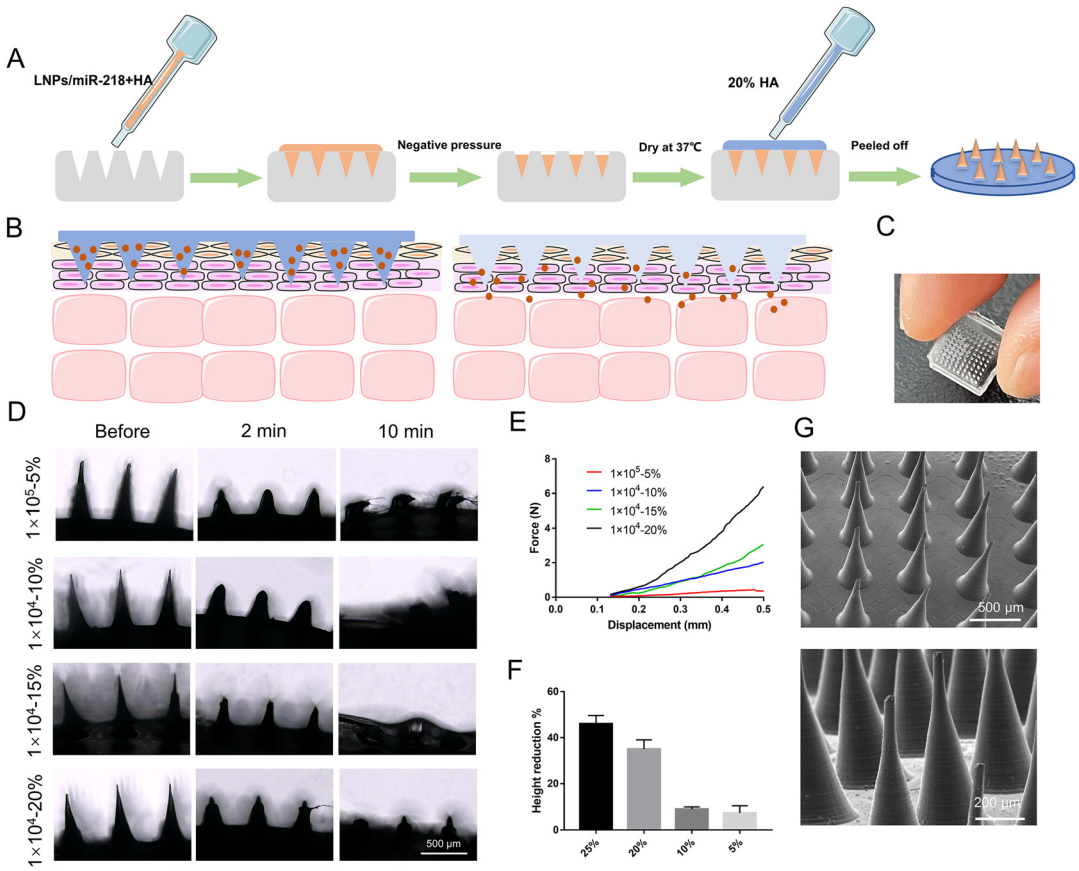

Fig. 3 Fabrication and characterization of MN/LPNs/miR-218. (A) Schematic representation of the fabrication process. (B) Transdermal application of MN/LPNs/miR-218, and (C) digital photo. (D) Side view of the MNs with different molecular weights or solubility of HA before and after insertion into the skin. (E) Characterization of the mechanical strength of MNs with different molecular weights or solubility of HA. (F) Comparison of the percentage height reduction of MNs with different LPNs/miR-218 content following the application of a force of 40 N. (G) SEM images of an MN in two different magnification times (scale bars = 500 or 200 μm). Data were shown as mean ± SD, n = 3.

resistance of MN with different contents of LPNs/miR-218 was detected to maximize the LPNs/miR-218 loading as well as to achieve sufficient mechanical strength. With the constant compression of 40 N, the height reduction percentage of MN tips was significantly reduced with the increasing of LPNs/miR-218 loading from 5% to 25% (w/w). Among all the groups, 5% and 10% LPNs/miR-218 loading groups displayed the height reduction percentage with a value of ~10% (Fig. 3F). In the previous reports, the needle height reduction percentage <10% represented acceptable mechanical strength.[42,43] Therefore, the MN patches constructed with 1×10^4 molecular weight HA in 20% solubility and at 10% loading of LPNs/miR-218 could be the excellent conditions for the candidates to deliver as many LPNs/miR-218 as possible to the skin. In an image of the 10 × 10 arrays, the MNs showed uniform and symmetric cone shapes with a height of 800 ± 25 μm, tip diameter of 30 ± 5 μm, and base diameter of 289 ± 19 μm (Fig. 3G).

3.4 Cutaneous permeation of MN

To assess the cutaneous penetration of MN, a fluorescent MN patch was fabricated with rhodamine B. As shown in Fig. S2A,† the red fluorescence was fully filled in the tips of the MN cavities, which confirmed that the cargo was loaded directly into the tip of the MN. After being implanted into the rat skin for 15 min, the puncture rate on the surface (red fluorescent spots/total tips number) was higher than 85%, implying the successful insertion into rat skin (Fig. S2B†). According to the histological analysis, the penetrated depth of MN was 678 ± 19 μm in rat skin, which was less than the height of MN (800 ± 25 μm) but was sufficient to reach the dermis layer (Fig. S2C†). We further compared the penetration capacity *in vivo* after the application of Gel/Cy5 and MN/Cy5. As shown in Fig. 4A, the Cy5 fluorescence intensity in both groups continuously increased for up to 30 min. However, the overall signal intensity generated by MN/Cy5 was notably higher than that produced by Gel/Cy5. The above results highlighted the superior penetration efficiency of MN.

The primary aim of this study was to deliver the MN-loaded cargo into the dermis layer where the hair follicles reside.[44] Therefore, it is crucial to analyze the drug distribution in different depths of the rat skin after MN or Gel administration. As shown in Fig. 4B, after incubation in Franz diffusion cells for different times either by topical smear Gel/Cy5 or implanted MN/Cy5 patched, the rat skin tissue were cryo-sec-

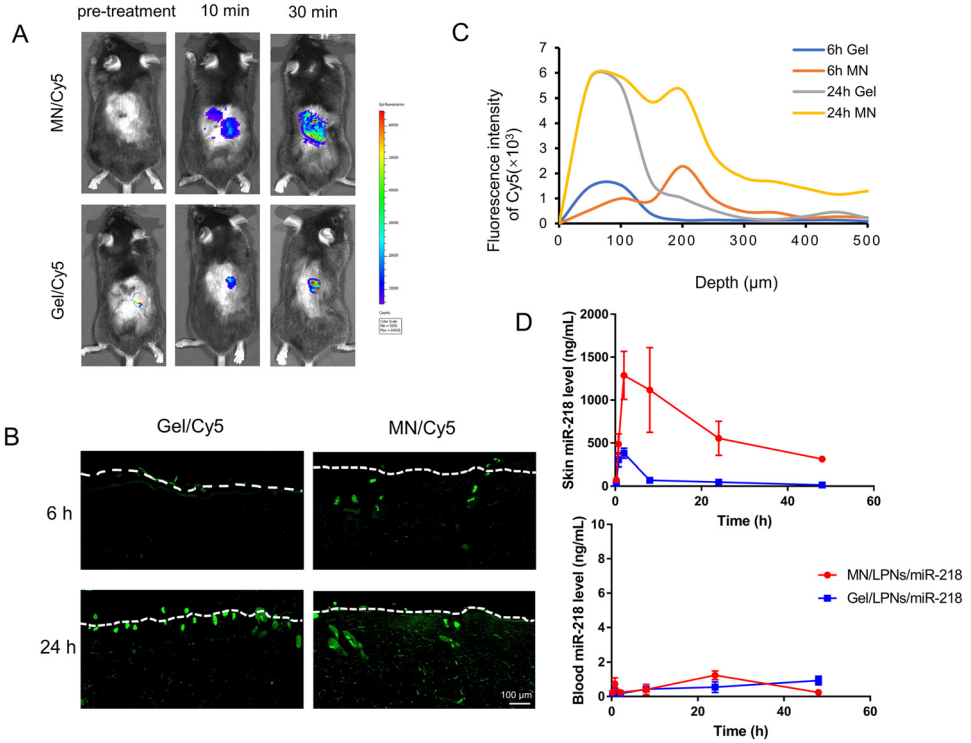

Fig. 4 Cutaneous penetration of MNs. (A) *In vivo* skin penetration test of MN/Cy5 and typical smear Gel/Cy5 at different times. (B) Cross-sectioned images and (C) fluorescence intensity statistics of rat skin after insertion of MN/Cy5 and typical smear Gel/Cy5 in 6 and 24 h (scale bars = 100 μm). (D) *In vivo* pharmacokinetic study results over 48 h application of MN/LPNs/miR-218 and Gel/LPNs/miR-218. Mature miR-218 concentration and time profile in skin and plasma (n = 3).

tioned and imaged by microscopy. It is well known that the epidermal thickness of the rat skin is around 40 μm, and the dermis is 30 to 40 times thicker than the epidermal.[45] In the MN/Cy5 group, the fluorescent signal passed through the epidermis and concentrated in the dermis layer in 6 h, furthermore, it obtained an increasing depth from the skin epidermis (white dotted line) to deep spatial distribution in 24 h. In the case of the Gel/Cy5 group, the feeble fluorescent signal mainly focused on the epidermis region in 6 h, after 24 hours of incubation, bits of fluorescent signals emerged in the dermal layer whereas most of it still concentrated in the epidermis (Fig. 4C). In summary, the significant advantage of the MN patch over topical smear administration was that it could pass through the stratum corneum and deliver the cargo into the dermis layer or deeper position of diffusion.

3.5 *In vivo* pharmacokinetic study

Since the miRNA treatment of alopecia required delivery of the miR-218 into the skin, the expression level of the mature miR-218 in the skin is vital for evaluating the delivery efficiency. Therefore, the *in vivo* pharmacokinetic study between MN/LPNs/miR-218 and Gel/LPNs/miR-218 was conducted to evaluate the mature miR-218 expression level in the skin and plasma after applying for different times. The expression of mature miR-218 was detected using the RT-qPCR method and the standard curve was constructed in the linear over the range of 0.069–690 000 ng mL^{-1} (Fig. S3†). After receiving the Gel/LPNs/miR-218 smear administration, the maximum mature miR-218 expression level in the skin (0.38 ± 0.06 μg mL^{-1}) was achieved at 1.58 ± 0.72 h, after that, it declined rapidly until 48 h. In another group, wherein the mice were implanted with the MN/LPNs/miR-218 patch, the expression level of the mature miR-218 increased quickly and reached a maximum of 1.33 ± 0.24 μg mL^{-1} after 6.02 ± 3.46 h of application. The maximum expression of the mature miR-218 in the MN/LPNs/miR-218 group was around 4-fold higher than that in the Gel/LPNs/miR-218 group. Meanwhile, the longer time to peak in the MN/LPNs/miR-218 group implicated the sustained release in the MN/LPNs system. After that, the skin mature miR-218 expression level of the MN/LPNs/miR-218 group decreased gradually to reach 0.31 ± 0.07 μg mL^{-1} on the last sampling point (48 h), which was still 23-fold higher than in the Gel/LPNs/miR-218 group (Fig. 4D). The higher expression of the miR-218 in the MN group in each sampling point confirmed a better penetration and higher bioavailability than the Gel smear administration in the skin, which was also demonstrated by the difference in mean residence time (MRT, 18.37 ± 1.63 *vs.* 11.25 ± 0.65 h) and the area under the drug concentration–time curve (AUC_{0-inf}, 32.3 ± 7.89 *vs.* 3.53 ± 0.29 μg g^{-1} h^{-1}) in the MN/LPNs/miR-218 group (Table 4). As shown in Fig. 4D, the pharmacokinetic profiles of mature miR-218 expression in plasma were administered at different times. The miR-218 expression maintained a low level in the plasma at each sampling point in the two groups

Table 4 Pharmacokinetic parameters after using MN/LPNs/miR-218 or Gel/LPNs/miR-218

Parameter	MN/LPNs/miR-218	Gel/LPNs/miR-218
t_{max} (h)	6.12 ± 3.46	1.58 ± 0.72
C_{max} (μg mL^{-1})	1.33 ± 0.24	0.38 ± 0.06
AUC_{0-inf} (μg g^{-1} h^{-1})	32.30 ± 7.89	3.53 ± 0.29
MRT (h)	18.37 ± 1.63	11.25 ± 0.65

where it reached one-thousandth of that in the skin indicating poor absorption of miR-218 into the systemic circulation. In summary, the dissolving MN/LPNs system was capable of delivering miR-218 locally in an efficient way and reducing systemic exposure, thus promoting miR-218 bioavailability.

3.6 *In vivo* effect of hair regrowth and security of MN/LPNs/miR-218 patches

To evaluate the efficacy in inducing hair regrowth, the hair loss therapy was studied using the 6–8-week-old shaved C57BL/6J mouse model at the telogen phase through MN/LPNs/miR-218 patches or Gel/LPNs/miR-218 smear administration. The sugaring hair removal method made the hair follicles enter the telogen phase and did not affect the normal cycle transformation, which is suitable to observe the hair follicle cycle and hair regrowth. Meanwhile, blank control and MN/LPNs/MSA patches were utilized as the control groups to confirm the independence of miR-218 in these treatment groups. Representative photographs of mice during the treatment were shown in Fig. 5A. After 1 d of hair removal, the pink color of the dorsal skin proved that the alopecia model was built successfully. Compared with the Gel/LPNs/miR-218 group, the treatment *via* MN/LPNs/miR-218 patches initiated a fast onset of hair regrowth in the two rounds of administration, which was reflected by pigmentation occurring on 5 d, while obvious hair regrowth was found on 13 d in the Gel/LPNs/miR-218 group. After 13 d of the administration, the regrowth hair uniformly covered the entire shaved region in the MN/LPNs/miR-218 treated mice. In contrast, in the Gel/LPNs/miR-218 group and other control groups, shaved regions

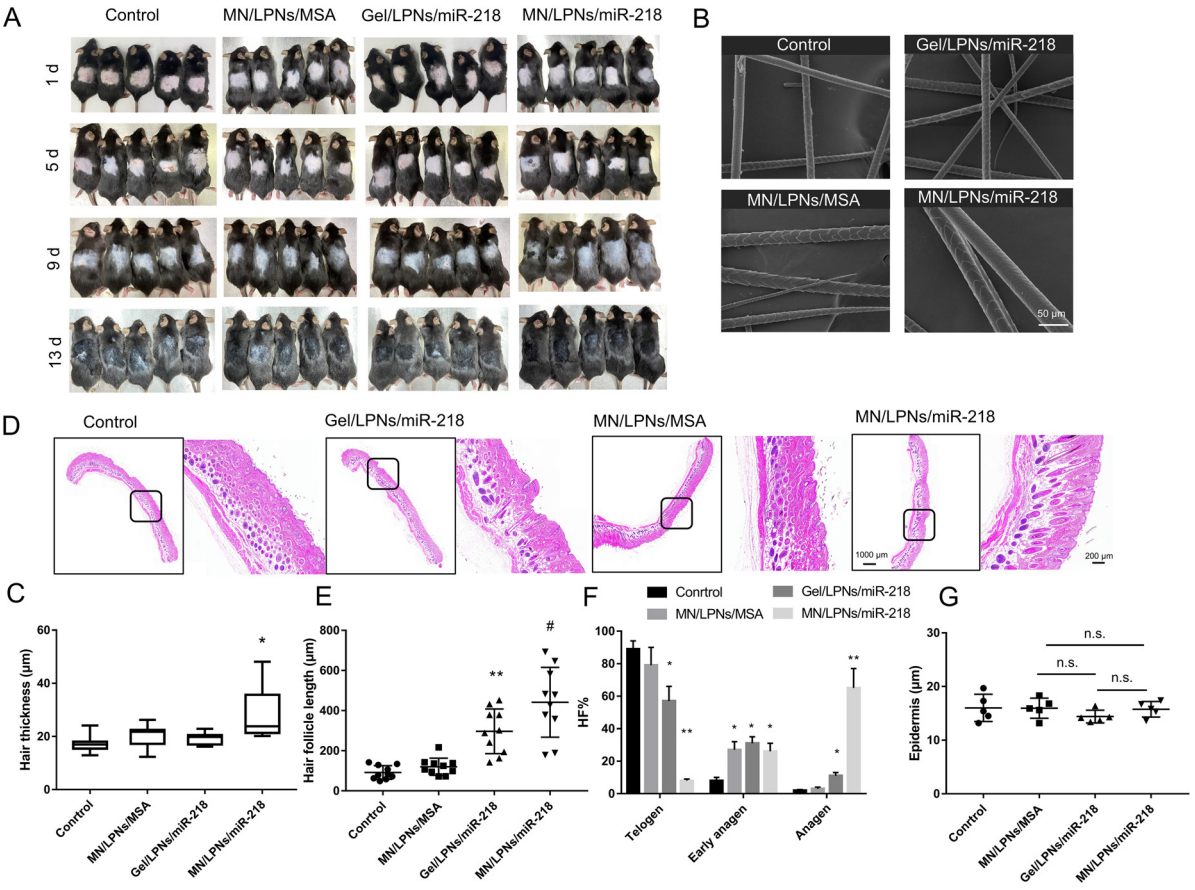

Fig. 5 *In vivo* evaluation of the MNs system for hair regrowth. (A) Photographs of hair regrowth in mouse model *via* MN/LPNs/miR-218 patch, topical Gel/LPNs/miR-218 smear administration at different times. (B) SEM images of hair after 13 days of treatment (scale bars = 50 μm). (C) Statistical result of hair thickness under SEM, $^{*}P < 0.05$ *vs.* Gel/LPNs/miR-218. (D) H&E staining of mouse skin after 13 days of treatment (scale bars = 1000 μm and 200 μm). Statistical result of hair follicle length (E), hair follicle proportion in different phases (F), and epidermis thickness (G) under H&E staining, $^{*}P < 0.05$, $^{**}P < 0.01$ *vs.* Control and $^{\#}P < 0.05$ *vs.* Gel/LPNs/miR-218. Data were shown as mean ± SD (n = 10), and statistical significance was calculated by one-way ANOVA followed by Dunnett's test.

were still observed. These results showed that MN/LPNs vector encapsulated miR-218 with a high efficiency, promoting hair regrowth over the entire region. The hair thickness of four groups was compared using scanning electron microscopy (SEM). The mean hair thickness (n = 10 per group) of MN/LPNs/miR-218 patch-administered mice (27.9 ± 9.4 μm) was significantly higher than that of the Gel/LPNs/miR-218 smear administration (19.3 ± 2.2 μm). However, there was no significant difference between the medians of the two groups because of the widely varied hair thickness in the MN/LPNs/miR-218 group, from 20.2 μm to 48.1 μm (Fig. 5B and C). SEM images revealed no damage on the surface of the regrown hair in each treatment group. Furthermore, after the administration of MN patches, the morphology of the hair follicle was confirmed by H&E staining in more detail (Fig. 5D). As shown in Fig. 5E, the mice treated with MN/LPNs/miR-218 possessed the highest length of the hair follicles among the four groups, followed by the Gel/LPNs/miR-218 group. As expected, more of the hair follicles in the MN/LPNs/miR-218 group remained in the anagen phase compared to the Gel/LPNs/miR-218 group which was revealed by an elongated morphology extending into the adipose layer.[46,47] Meanwhile, the telogen phase proportion of the hair follicles in the MN/LPNs/miR-218 group was significantly inhibited, which demonstrated that the MN/LPNs/miR-218 group promoted telogen-to-anagen transition more effectively than in the topical administration group. In addition, compared with the hair follicles in the control group which exhibited an oval shape in the corium layer, MN/LPNs/MSA could also promote the hair follicles' transition to the early anagen phase (Fig. 5F). This phenomenon might be due to the promotion of proliferation and migration of HA on DP cells.[48]

The security of MN patches was confirmed by the skin recovery test and normal epidermis properties. As shown in Fig. S4,† after 30 s of constant pressure, the outline of MN and even the indentation of tips was clearly visible and fully recovered after 3 min with neither irritation nor erythema. Furthermore, to verify the normal epidermal properties after MN patches and Gel smear application, the epidermal thickness was measured in each group. The epidermis was around 15 μm thick and with no significant differences within groups (Fig. 5G). Altogether, these data implied that MN/LPNs/miR-218 patches effectively delivered miR-218 to the skin in the dermis layer elevated hair regrowth by accelerating the telogen-anagen transition without damaging the hair follicles or the epidermis layer.

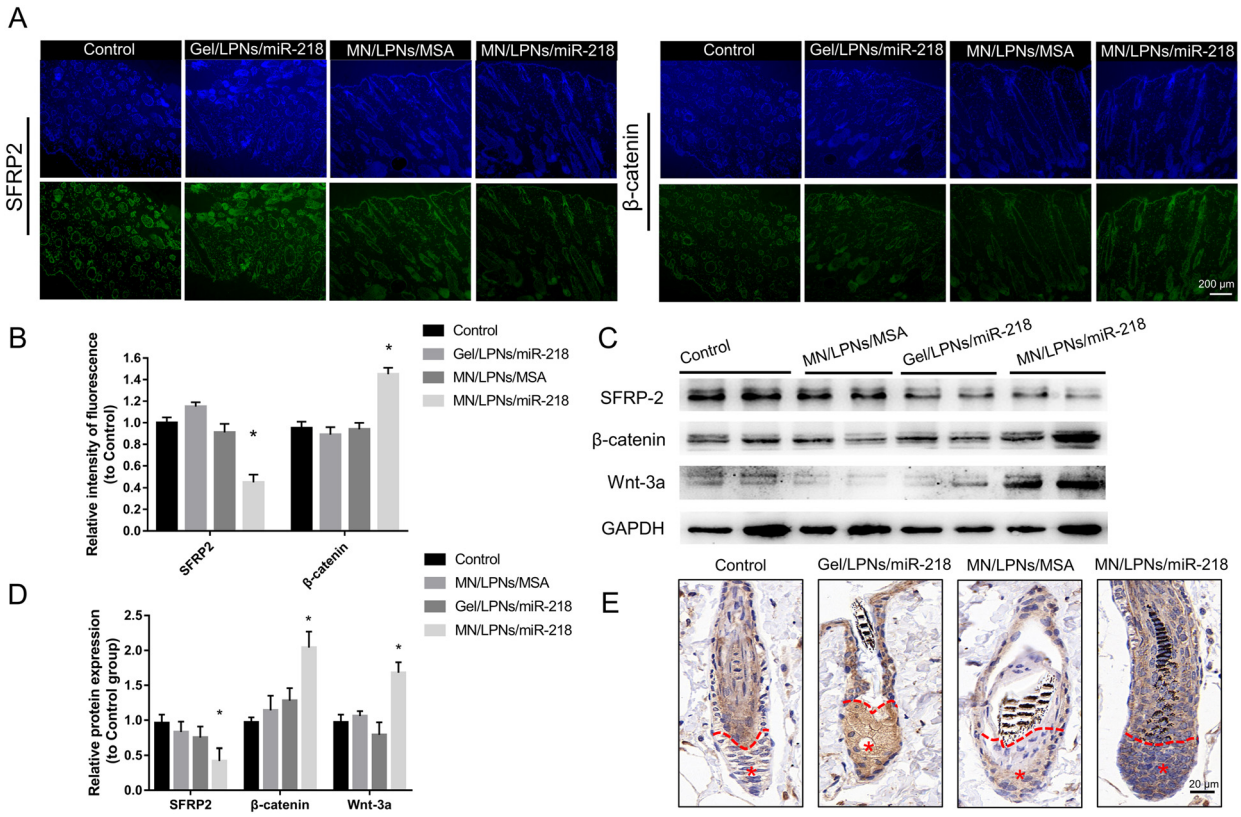

Fig. 6 *In vivo* evaluation of the regulation of MN/LPNs-miR-218 on Wnt/β-catenin channel. (A) Immunofluorescence of β-cantenin and SFRP2 on the skin after 13 days of treatment (scale bars = 200 μm). (B) Statistical result of fluorescence intensity. (C) Western blot and (D) statistical result of Wnt/β-catenin channel markers and miR-218 target gene in the skin after 13 days treatment, *P < 0.05 *vs.* Gel/LPNs/miR-218. (E) Immunohistochemical of versican on the skin after 13 days treatment (*: DP aggregates, scale bars = 20 μm). Data were shown as mean ± SD (n = 5), and statistical significance was calculated by one-way ANOVA followed by Dunnett's test.

3.7 *In vivo* regulation of MN/LPNs/miR-218 on Wnt/β-catenin

To verify the effect of the Wnt/β-catenin channel after MN/LPNs/miR-218 or Gel/LPNs/miR-218 administration, firstly, we conducted immunofluorescence analysis of β-catenin and SFRP2 expression in the shaved skin after 13 days of treatment (Fig. 6A and B). Quantitative analysis of staining images showed that the MN/LPNs/miR-218 group brought the highest expression level of β-catenin, which is an essential protein of DP cells proliferation in hair follicles regions at around 1.57-fold of the control group, followed by the Gel/LPNs/miR-218 smear group (~0.91-fold of the control group). SFRP2, a miR-218 target gene and a negative regulator of the Wnt/β-catenin channel, was remarkably more suppressed in the MN/LPNs/miR-218 group compared to other groups. Then, western blot analysis revealed that the protein expression level of β-catenin and SFRP2 were consistent with immunofluorescence results in two mice of each group. Gray scanning quantitative analysis showed a significantly higher expression of β-catenin and Wnt-3a in the MN/LPNs/miR-218 group than that in the Gel/LPNs/miR-218 group. Similarly, the lowest expression of SFRP2 was detected in the MN/LPNs/miR-218 group followed by the Gel/LPNs/miR-218 group (Fig. 6C and D). As a marker protein of DP cells, versican has an important role in inducing hair follicle regeneration, which is highly expressed in dermal papilla during the anagen phase and obviously decreased in the catagen phase.[49,50] As shown in Fig. 6E, compared with the control and MN/LPNs/MSA groups, the miR-218 treatment groups showed higher expression of versican in the dermal papilla region (* region). Especially, the number of the versican-positive DP cells in the MN/LPNs/miR-218 group was higher than that in the Gel/LPNs/miR-218 group, which indicated the impact of miR-218 in promoting the proliferation of DP cells and the higher effect in the MN/LPNs/miR-218 group. The above results suggest that implantation of MN/LPNs/miR-218 patches could activate the Wnt/β-catenin channel by inhibiting SFRP2 more effectively than a topical smear of Gel/LPNs/miR-218, further promoting DP cell proliferation.

4. Conclusion

This study introduced an HA-based dissolving MN patch loaded with LPNs/miR-218 for hair regrowth. Meanwhile, it suggested that the combination of MN with LPNs offers great potential for the successful localization and sustaining transdermal delivery of miRNA. The fabricated MN/LPNs/miR-218 patches possessed enough mechanical strength to pass through the corneum, and LPNs/miR-218 had a micron size range and favorable stability to protect from degradation before reaching the destination. *Ex vivo* skin insertion revealed that MN patches could penetrate the corneum and facilitate drug deposition mainly in the dermis layer. Moreover, the pharmacokinetic studies demonstrated that MN patches yielded very limited systemic exposure in the plasma. Once MN/LPNs/miR-218 was applied, it could maintain a high miR-218 level in the administration site and increase the bioavailability of miR-218 compared with the topical administration. Finally, in *in vivo* experiments, MN/LPNs/miR-218 patches induced a more effective hair regrowth than topical administration by promoting the telogen-anagen phase transition of the hair follicle. Overall, this dissolving MN/LPN device provided an effective strategy for the miRNA transdermal delivery of alopecia.

Author contributions

Yipu Zhao: conceptualization, methodology, investigation, visualization, software, formal analysis, data curation, writing – original draft, writing – review & editing. Ye Tian: conceptualization, supervision. Weiliang Ye: writing – review & editing, conceptualization, investigation. Xue Wang: animal experiments, writing – review & editing. Ying Huai: animal experiments. Qian Huang: animal experiments. Xiaohua Chu: writing – review & editing. Xudong Deng: investigation, visualization, validation. Airong Qian: conceptualization, supervision, project administration, writing – review & editing, resources, funding acquisition.

Conflicts of interest

No potential conflict of interest was reported by the authors.

Acknowledgements

This work was funded by grants from the National Natural Science Foundation of China (No. 21805229), Shaanxi Provincial Key R&D Program (No. 2021GXLH-01-02, No. 2021SF-293, No. 2022KWZ-13), the Fundamental Research Funds for the Central Universities (No. 3102019smxy003).

References

1 N. Meah, D. Wall, K. York, B. Bhoyrul, L. Bokhari, D. Asz-Sigall, W. F. Bergfeld, R. C. Betz, U. Blume-Peytavi, V. Callender, V. Chitreddy, A. Combalia, G. Cotsarelis, B. Craiglow, J. Donovan, S. Eisman, P. Farrant, J. Green, R. Grimalt, M. Harries, M. Hordinsky, A. D. Irvine, S. Itami, V. Jolliffe, B. King, W. S. Lee, A. McMichael, A. Messenger, P. Mirmirani, E. Olsen, S. J. Orlow, B. M. Piraccini, A. Rakowska, P. Reygagne, J. L. Roberts, L. Rudnicka, J. Shapiro, P. Sharma, A. Tosti, A. Vogt, M. Wade, L. Yip, A. Zlotogorski and R. D. Sinclair, *J. Am. Acad. Dermatol.*, 2021, **84**, 1594–1601.
2 A. Adil and M. Godwin, *J. Am. Acad. Dermatol.*, 2017, **77**, 136–141.
3 A. K. Gupta, M. Venkataraman, M. Talukder and M. A. Bamimore, *JAMA Dermatol.*, 2022, **158**, 266–274.
4 M. Avram and N. Rogers, *Dermatol. Surg.*, 2009, **35**, 1705–1719.
5 A. K. Gupta and A. Charrette, *Skinmed*, 2015, **13**, 185–189.
6 T. Andl and N. V. Botchkareva, *Exp. Dermatol.*, 2015, **24**, 821–826.

7 T. S. Purba, L. Brunken, N. J. Hawkshaw, M. Peake, J. Hardman and R. Paus, *Exp. Dermatol.*, 2016, **25**, 663–668.
8 Y. C. Hsu, H. A. Pasolli and E. Fuchs, *Cell*, 2011, **144**, 92–105.
9 L. Alonso and E. Fuchs, *J. Cell Sci.*, 2006, **119**, 391–393.
10 J. Ohn, K. H. Kim and O. Kwon, *J. Dermatol. Sci.*, 2019, **93**, 144–149.
11 B. Zhao, Y. Chen, N. Yang, Q. Chen, Z. Bao, M. Liu, S. Hu, J. Li and X. Wu, *J. Cell Physiol.*, 2019, **234**, 20329–20341.
12 S. Hu, Z. Li, H. Lutz, K. Huang, T. Su, J. Cores, P. C. Dinh and K. Cheng, *Sci. Adv.*, 2020, **6**, eaba1685.
13 J. Cabral, A. E. Ryan, M. D. Griffin and T. Ritter, *Adv. Drug Delivery Rev.*, 2018, **129**, 394–406.
14 S. Y. Wang, H. Kim, G. Kwak, S. D. Jo, D. Cho, Y. Yang, I. C. Kwon, J. H. Jeong and S. H. Kim, *Theranostics*, 2020, **10**, 3240–3253.
15 B. Mandal, H. Bhattacharjee, N. Mittal, H. Sah, P. Balabathula, L. A. Thoma and G. C. Wood, *Nanomedicine*, 2013, **9**, 474–491.
16 R. X. Zhang, T. Ahmed, L. Y. Li, J. Li, A. Z. Abbasi and X. Y. Wu, *Nanoscale*, 2017, **9**, 1334–1355.
17 S. Sabnis, E. S. Kumarasinghe, T. Salerno, C. Mihai, T. Ketova, J. J. Senn, A. Lynn, A. Bulychev, I. McFadyen, J. Chan, O. Almarsson, M. G. Stanton and K. E. Benenato, *Mol. Ther.*, 2018, **26**, 1509–1519.
18 A. Gabizon, Y. Amitay, D. Tzemach, J. Gorin, H. Shmeeda and S. Zalipsky, *J. Controlled Release*, 2012, **160**, 245–253.
19 Q. Sun, X. Sun, X. Ma, Z. Zhou, E. Jin, B. Zhang, Y. Shen, E. A. Van Kirk, W. J. Murdoch, J. R. Lott, T. P. Lodge, M. Radosz and Y. Zhao, *Adv. Mater.*, 2014, **26**, 7615–7621.
20 Y. Zhu, M. Lin, W. Hu, J. Wang, Z. G. Zhang, K. Zhang, B. Yu and F. J. Xu, *Angew. Chem., Int. Ed.*, 2022, **61**, e202200535.
21 M. Z. Wang, Y. Xu, J. F. Xie, Z. H. Jiang and L. H. Peng, *Biomater. Sci.*, 2021, **9**, 8373–8385.
22 J. Arya, S. Henry, H. Kalluri, D. V. McAllister, W. P. Pewin and M. R. Prausnitz, *Biomaterials*, 2017, **128**, 1–7.
23 Y. Ye, J. Yu, D. Wen, A. R. Kahkoska and Z. Gu, *Adv. Drug Delivery Rev.*, 2018, **127**, 106–118.
24 C. Tas, J. C. Joyce, H. X. Nguyen, P. Eangoor, J. S. Knaack, A. K. Banga and M. R. Prausnitz, *J. Controlled Release*, 2017, **268**, 159–165.
25 M. Jang, B. M. Kang, H. Yang, J. Ohn, O. Kwon and H. Jung, *Adv. Healthc. Mater.*, 2021, **10**, e2001691.
26 G. Yang, Q. Chen, D. Wen, Z. Chen, J. Wang, G. Chen, Z. Wang, X. Zhang, Y. Zhang, Q. Hu, L. Zhang and Z. Gu, *ACS Nano*, 2019, **13**, 4354–4360.
27 M. R. Prausnitz, *Adv. Drug Delivery Rev.*, 2004, **56**, 581–587.
28 S. Duarah, M. Sharma and J. Wen, *Eur. J. Pharm. Biopharm.*, 2019, **136**, 48–69.
29 A. J. Mieszawska, A. Gianella, D. P. Cormode, Y. Zhao, A. Meijerink, R. Langer, O. C. Farokhzad, Z. A. Fayad and W. J. Mulder, *Chem. Commun.*, 2012, **48**, 5835–5837.
30 M. F. Kramer, *Curr. Protoc. Mol. Biol.*, 2011, ch. 15, unit 15 10.
31 H. Yang, S. Kim, G. Kang, S. F. Lahiji, M. Jang, Y. M. Kim, J. M. Kim, S. N. Cho and H. Jung, *Adv. Healthc. Mater.*, 2017, **6**, 19.
32 N. M. Belliveau, J. Huft, P. J. Lin, S. Chen, A. K. Leung, T. J. Leaver, A. W. Wild, J. B. Lee, R. J. Taylor, Y. K. Tam, C. L. Hansen and P. R. Cullis, *Mol. Ther.–Nucleic Acids*, 2012, **1**, e37.
33 Y. Tian, Y. Zhao, C. Yin, S. Tan, X. Wang, C. Yang, T. D. Zhang, X. Zhang, F. Ye, J. Xu, X. Wu, L. Ding, J. Zhang, J. Pei, X. T. Wang, R. X. Zhang, J. Xu, W. Wang, C. D. M. Filipe, T. Hoare, D. C. Yin, A. Qian and X. Deng, *J. Controlled Release*, 2022, **345**, 20–37.
34 M. A. A. Jansen, L. H. Klausen, K. Thanki, J. Lyngso, J. Skov Pedersen, H. Franzyk, H. M. Nielsen, W. van Eden, M. Dong, F. Broere, C. Foged and X. Zeng, *Eur. J. Pharm. Biopharm.*, 2019, **142**, 38–48.
35 H. Y. Xue and H. L. Wong, *ACS Nano*, 2011, **5**, 7034–7047.
36 K. Laxman, B. P. K. Reddy, S. K. Mishra, M. B. Gopal, A. Robinson, A. De, R. Srivastava and M. Ravikanth, *ACS Appl. Mater. Interfaces*, 2020, **12**, 52329–52342.
37 V. D. Bui, S. Son, W. Xavier, V. Q. Nguyen, J. M. Jung, J. Lee, S. Shin, W. Um, J. Y. An, C. H. Kim, Y. Song, Y. Li and J. H. Park, *Biomaterials*, 2022, **287**, 121644.
38 H. Shi, J. Zhou, Y. Wang, Y. Zhu, D. Lin, L. Lei, S. Vakal, J. Wang and X. Li, *Small*, 2022, **18**, e2104657.
39 M. Leone, S. Romeijn, B. Slutter, C. O'Mahony, G. Kersten and J. A. Bouwstra, *Eur. J. Pharm. Sci.*, 2020, **146**, 105269.
40 Y. Chi, Y. Huang, Y. Kang, G. Dai, Z. Liu, K. Xu and W. Zhong, *Eur. J. Pharm. Sci.*, 2022, **168**, 106075.
41 S. Kim, J. Eum, H. Yang and H. Jung, *J. Controlled Release*, 2019, **316**, 1–11.
42 A. D. Permana, I. A. Tekko, M. T. C. McCrudden, Q. K. Anjani, D. Ramadon, H. O. McCarthy and R. F. Donnelly, *J. Controlled Release*, 2019, **316**, 34–52.
43 B. Pamornpathomkul, T. Ngawhirunpat, I. A. Tekko, L. Vora, H. O. McCarthy and R. F. Donnelly, *Eur. J. Pharm. Sci.*, 2018, **121**, 200–209.
44 L. A. Garza, C. C. Yang, T. Zhao, H. B. Blatt, M. Lee, H. He, D. C. Stanton, L. Carrasco, J. H. Spiegel, J. W. Tobias and G. Cotsarelis, *J. Clin. Invest.*, 2011, **121**, 613–622.
45 L. Diaz-Gomez, I. Gonzalez-Prada, R. Millan, A. Da Silva-Candal, A. Bugallo-Casal, F. Campos, A. Concheiro and C. Alvarez-Lorenzo, *Carbohydr. Polym.*, 2022, **278**, 118924.
46 J. W. Oh, J. Kloepper, E. A. Langan, Y. Kim, J. Yeo, M. J. Kim, T. C. Hsi, C. Rose, G. S. Yoon, S. J. Lee, J. Seykora, J. C. Kim, Y. K. Sung, M. Kim, R. Paus and M. V. Plikus, *J. Invest. Dermatol.*, 2016, **136**, 34–44.
47 S. Muller-Rover, B. Handjiski, C. van der Veen, S. Eichmuller, K. Foitzik, I. A. McKay, K. S. Stenn and R. Paus, *J. Invest. Dermatol.*, 2001, **117**, 3–15.
48 M. J. Kim, K. Y. Seong, D. S. Kim, J. S. Jeong, S. Y. Kim, S. Lee, S. Y. Yang and B. S. An, *Acta Biomater.*, 2022, **143**, 189–202.
49 J. Wang, Y. Miao, Y. Huang, B. Lin, X. Liu, S. Xiao, L. Du, Z. Hu and M. Xing, *Adv. Healthc. Mater.*, 2018, **7**, 3.
50 J. Kishimoto, R. Ehama, L. Wu, S. Jiang, N. Jiang and R. E. Burgeson, *Proc. Natl. Acad. Sci. U. S. A.*, 1999, **96**, 7336–7341.

